



## Absence of Weyl nodes in $\text{EuCd}_2\text{As}_2$ revealed by the carrier density dependence of the anomalous Hall effect

Yue Shi,<sup>1,2</sup> Zhaoyu Liu,<sup>1</sup> Logan A. Burnett,<sup>3</sup> Seokhyeong Lee,<sup>4</sup> Chaowei Hu,<sup>1</sup> Qianni Jiang,<sup>1</sup> Jiaqi Cai ,<sup>1</sup> Xiaodong Xu,<sup>1,2</sup> Mo Li,<sup>1,4</sup> Cheng-Chien Chen,<sup>3</sup> and Jiun-Haw Chu <sup>1</sup>

<sup>1</sup>*Department of Physics, University of Washington, Seattle, Washington 98195, USA*

<sup>2</sup>*Department of Materials Science and Engineering, University of Washington, Seattle, Washington 98195, USA*

<sup>3</sup>*Department of Physics, University of Alabama at Birmingham, Birmingham, Alabama 35294, USA*

<sup>4</sup>*Department of Electrical and Computer Engineering, University of Washington, Seattle, Washington 98195, USA*



(Received 2 February 2024; accepted 4 March 2024; published 26 March 2024)

The antiferromagnetic layered compound  $\text{EuCd}_2\text{As}_2$  is widely considered a leading candidate of ideal Weyl semimetals, featuring a single pair of Weyl nodes in its field-induced ferromagnetic state. Nevertheless, this view was recently challenged by an optical spectroscopy study, which suggested that it is a magnetic semiconductor. In this study, we successfully synthesized highly insulating  $\text{EuCd}_2\text{As}_2$  crystals with carrier density reaching as low as  $2 \times 10^{15} \text{ cm}^{-3}$ . The magnetotransport measurements revealed a progressive decrease of the anomalous Hall conductivity (AHC) by several orders of magnitude as the carrier density decreases. This behavior contradicts what is expected from the intrinsic AHC generated by the Weyl points, which is independent of carrier density as the Fermi level approaches the charge neutrality point. In contrast, the scaling relationship between AHC and longitudinal conductivity aligns with the characteristics of variable-range hopping insulators. Our results suggest that  $\text{EuCd}_2\text{As}_2$  is a magnetic semiconductor rather than a topological Weyl semimetal.

DOI: [10.1103/PhysRevB.109.125202](https://doi.org/10.1103/PhysRevB.109.125202)

### I. INTRODUCTION

Weyl semimetals have attracted significant attention due to their intriguing electronic properties arising from the presence of Weyl points [1,2]. Among them, ideal magnetic Weyl semimetals, characterized by a single pair of Weyl points close to the Fermi level, have long been sought for exploring the intrinsic topological effects associated with Weyl fermions free from interference by other trivial energy bands. In the past few years, the layered magnetic compound  $\text{EuCd}_2\text{As}_2$  was proposed to be one of the leading candidates to realize an ideal magnetic Weyl semimetal in its field-induced ferromagnetic (FM) state [3–5].  $\text{EuCd}_2\text{As}_2$  has a hexagonal unit cell with space group  $P-3m1$  [No. 164; Fig. 1(a)]. At a temperature of 9.5 K, the localized magnetic moments of Eu develop a long-range magnetic order, with moments ferromagnetically coupled within layers and antiferromagnetically coupled between layers [6–8]. Nevertheless, the magnetic ground state appears to be highly tunable and depends on the growth method and the application of a small amount of hydrostatic pressure [9–11]. Application of a 2 T magnetic field saturates all magnetic moments along the  $c$  axis at low temperature, stabilizing a field-induced FM state. Previous density functional theory (DFT) calculations suggested that Cd  $s$  and As  $p$  orbitals are inverted near the  $\Gamma$  point in the energy bands of  $\text{EuCd}_2\text{As}_2$  [7,12], leading to an antiferromagnetic (AFM) topological insulator. Once the moments are fully saturated along the  $c$  axis in the FM state, the Zeeman splitting lifts the band degeneracy and gives rise to a single pair of Weyl points [3–5].

In previous works, a high magnetic field quantum oscillation study revealed a small Fermi surface with a light

effective mass in the field-induced FM state of  $\text{EuCd}_2\text{As}_2$  [3]; a Hall resistivity study presented a large anomalous Hall conductivity at low temperatures presumably related to the topological state of  $\text{EuCd}_2\text{As}_2$  [3,13–15], and angle-resolved photoemission spectroscopy experiments observed the quasi-linear dispersion of the valence band in the AFM state and the band degeneracy splitting at a temperature right above the Néel temperature due to the existence of strong spin fluctuations [5,16,17]. All of these observations seem to agree with the existence of the Weyl semimetal phase. Nevertheless, the direct observation of Weyl crossings of  $\text{EuCd}_2\text{As}_2$  is not possible because all the samples synthesized so far are  $p$  type with a Fermi level below the valence band top. In contrast, a recent study employing optical conductivity and pump-probe photoemission suggested that  $\text{EuCd}_2\text{As}_2$  is, in fact, a semiconductor with an electronic gap of 0.77 eV instead of a Weyl semimetal [18]. Furthermore, a systematic investigation of the DFT calculation of the materials family  $\text{EuCd}_2\text{X}_2$  ( $X=\text{P, As, Sb, Bi}$ ) revealed that the topological states of materials in this family are sensitive to the choice of functional and the value of Hubbard  $U$ ; hence, the conduction and valence bands might not even be inverted in  $\text{EuCd}_2\text{As}_2$  [19].

A well-known prediction for a type-I Weyl semimetal is that the anomalous Hall conductivity (AHC) is solely determined by the distance between the Weyl nodes in the momentum space when the Fermi level is exactly at the Weyl crossings [20,21]. Therefore, the AHC is expected to approach a finite and constant value as carrier density decreases to zero, which serves as direct evidence to distinguish Weyl semimetals from other trivial electronic states. In this work, we successfully synthesize  $\text{EuCd}_2\text{As}_2$  single crystals with carrier density ranging from  $10^{15}$  to  $10^{16} \text{ cm}^{-3}$  in the

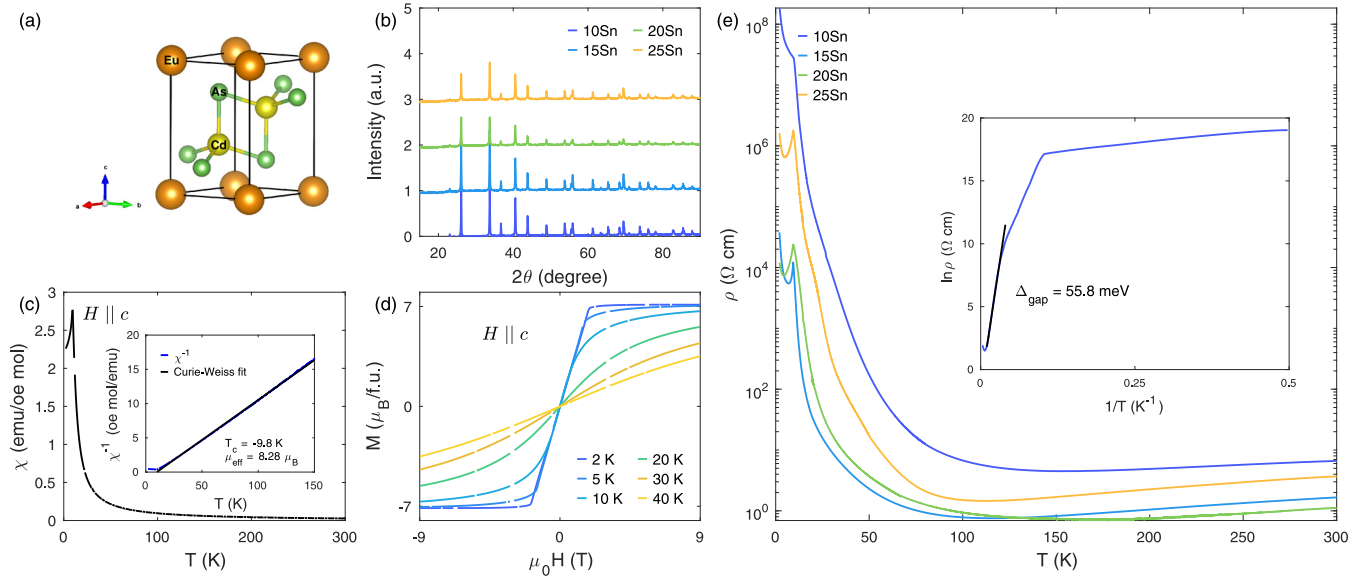


FIG. 1. Transport and magnetic characterizations of  $\text{EuCd}_2\text{As}_2$ . (a) Crystal structure of  $\text{EuCd}_2\text{As}_2$  with the  $P\text{-}3m1$  space group. (b) Powder x-ray diffraction of  $\text{EuCd}_2\text{As}_2$  at room temperature. (c) Temperature dependence of magnetic susceptibility  $\chi$  with 0.1 T magnetic field applied along the  $c$  axis. The inset shows the inverse susceptibility versus temperature and the Curie-Weiss fitting. (d) Magnetization versus field at different temperatures. The saturated magnetization is  $\sim 7\mu_B$  per Eu atom at the base temperature 2 K. (e) Temperature dependence of the electrical resistivity  $\rho(T)$  between 2 and 300 K. The inset shows  $\ln \rho$  versus the inverse of temperature  $1/T$  of the sample from 10Sn. The transport activation gap  $\Delta_{\text{gap}} = 55.8$  meV is obtained by fitting  $\ln \rho$  versus  $1/T$  in the temperature range of 30–100 K.

field-induced FM state and conducted a systematic study of the transport behaviors of these samples. We find that the temperature dependence of resistivity of all samples shows an insulating behavior and the resistivity dramatically decreases by several orders of magnitude as Eu moments are fully saturated by a  $c$ -axis magnetic field. We find the AHC decreases by several orders of magnitude as the carrier density decreases, far below the value expected from previous DFT calculations that predicted a Weyl semimetal phase in this system. In contrast, the scaling analysis shows good agreement with the AHC in the variable-range hopping regime. The optical transmittance measurement further confirms a finite optical gap of 0.74 eV, consistent with previous studies. An *ab initio* calculation to compute the Hubbard  $U$  parameter of  $\text{EuCd}_2\text{As}_2$  is also performed in this work, revealing that previous calculations significantly underestimate the value of Hubbard  $U$ , highlighting the importance of correlation when determining the topological phase of magnetic semiconductors.

## II. RESULTS

### A. Transport and magnetic characterization

$\text{EuCd}_2\text{As}_2$  single crystals were synthesized via the Sn flux method [9]. We discovered that the residual carrier density of crystals is sensitive to the Sn flux ratio. The stoichiometric Eu pieces and Cd and As shots are mixed with 10 to 25 times atomic mass Sn shots as starting materials, which yielded  $\text{EuCd}_2\text{As}_2$  crystals with the hole carrier density spanning from  $10^{15}$  to  $10^{16}$   $\text{cm}^{-3}$ . While it is unclear how the Sn flux ratio alters the defect density, the wide range of carrier density offers us a convenient knob to tune the transport properties of  $\text{EuCd}_2\text{As}_2$ .

Figure 1(b) shows the powder x-ray diffraction of  $\text{EuCd}_2\text{As}_2$  samples from batches using 10, 15, 20, and 25 Sn flux ratios (labeled 10Sn, 15Sn, 20Sn, and 25Sn). All diffraction patterns and extracted lattice constants are identical to the previous report [9], indicating that the change in the Sn flux ratio has a minimal effect on structural properties. Similarly, the magnetic properties of samples from different batches show no measurable difference and agree with previous studies [5]. The representative data of a sample from 10Sn are summarized in Fig. 1. As shown in Fig. 1(c), the temperature dependence of  $c$ -axis magnetic susceptibility  $\chi$  follows the Curie-Weiss temperature dependence, with a kink at 9.5 K indicating the onset of AFM order. Fitting the high-temperature susceptibility with the Curie-Weiss law yields a Weiss temperature of  $-9.8$  K and an effective magnetic moment of  $8.28\mu_B$ . Figure 1(d) shows the magnetization  $\mathbf{M}$  as a function of the field measured at different temperatures. At the base temperature of 2 K,  $\mathbf{M}$  increases linearly before reaching the saturated value of  $\sim 7\mu_B$  per Eu atom, in agreement with the magnetic moment of a divalent Eu with half-filled  $4f$  orbitals.

Unlike the structural and magnetic properties, the electrical transport of  $\text{EuCd}_2\text{As}_2$  is very sensitive to the Sn flux ratio. Figure 1(e) shows the temperature dependence of in-plane resistivity  $\rho(T)$  for samples selected from different batches. All samples show an insulating behavior below 100 K, where resistivity increases by 3 to 7 orders of magnitude as the temperature decreases. This is very different from the semimetal behavior reported in previous studies [3,13,14], with the exception of the most recent works [18,22]. The kink in resistivity at 9.5 K is consistent with the AFM transition determined from the magnetic susceptibility. Below 9.5 K the resistivity of the sample from 10Sn continuously increases,

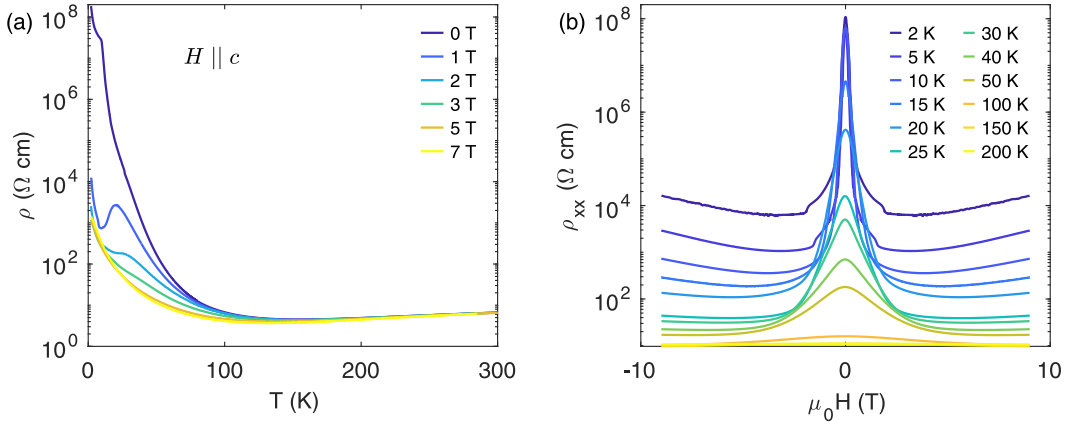


FIG. 2. Colossal magnetoresistance of  $\text{EuCd}_2\text{As}_2$ . (a) Temperature dependence of resistivity  $\rho(T)$  under different magnetic fields applied along the  $c$  axis. (b) Resistivity  $\rho_{xx}$  versus magnetic field at temperatures between 2 and 200 K.

while samples from 15Sn, 20Sn, and 25Sn initially decrease before increasing again as the temperature cools further down to 2 K. The inset in Fig. 1(e) shows  $\ln \rho$  versus  $1/T$  of the sample from 10Sn. The black solid line denotes the linear fit of  $\ln \rho$  versus  $1/T$  in the temperature range between 30 and 100 K, which allows us to extract the activation energy  $\Delta_{\text{gap}} \sim 55.8$  meV using the relationship  $\ln \rho = \frac{\Delta_{\text{gap}}}{2k_B T}$ . We note that in a disordered semiconductor the activation energy extracted from resistivity is often related to the energy of impurity levels, which is much lower than the band gap.

### B. Colossal magnetoresistance

The insulating resistivity of  $\text{EuCd}_2\text{As}_2$  can be strongly modulated by the application of magnetic fields. The magnetoresistance (MR) of the sample from 10Sn is summarized in Fig. 2. The results are qualitatively similar to samples from other batches. Figure 2(a) shows the temperature dependence of the resistivity  $\rho(T)$  under different magnetic fields from 0 to 7 T. The exponential increase of resistivity is suppressed by the external magnetic field, resulting in a dramatic decrease of resistivity by almost 5 orders of magnitude. As the magnetic field increases, the kink at the Néel temperature is smeared, and a bumplike feature at  $\sim 20$  K emerges for 1 T magnetic field and then shifts to the higher temperatures. For temperatures higher than 100 K, where resistivity no longer follows the thermally activated temperature dependence, the magnetoresistance becomes negligible.

Figure 2(b) shows the magnetoresistivity  $\rho_{xx}$  as a function of field at a fixed temperature between 2 and 200 K. It can be seen that at low temperatures resistivity abruptly drops by several orders of magnitude as magnetic field increases, followed by a kink at the saturation field, above which the resistivity increases again when magnetic moments are fully aligned with the field. As temperature increases, the drop in resistivity becomes more gradual, and the kink is smeared out, which is highly correlated with the field dependence of magnetization at higher temperatures [Fig. 1(d)]. This was also reported in a recent work [22] and is consistent with the decrease in band gap induced by the saturation of magnetization reported in Ref. [18].  $\text{MR} = 100\% \times [\rho_{xx}(9\text{T}) - \rho_{xx}(0\text{T})]/\rho_{xx}(0\text{T})$  reaches  $-90\%$  at  $T < 50$  K. Such a colossal

negative MR was also observed in several Eu-based semiconducting materials, a property that might be of interest for spintronics applications [23,24].

### C. Anomalous Hall effect

The Hall resistivity  $\rho_{xy}$  is shown in Fig. 3(a) for samples from 10Sn, 15Sn, and 20Sn. Similar to the longitudinal resistivity  $\rho_{xx}$ ,  $\rho_{xy}$  is strongly affected by the magnetism. As temperature decreases, the field dependence of  $\rho_{xy}$  becomes highly nonlinear and resembles that of the magnetization, a clear sign of the anomalous Hall effect (AHE). For temperatures below 10 K,  $\rho_{xx}$  becomes too large (approximately  $\text{M}\Omega \text{ cm}$ ) for magnetic fields below 2 T, so antisymmetrization becomes too difficult to extract  $\rho_{xy}$ , and hence, only data above 2 T are presented. To quantitatively understand the temperature and carrier density dependence of the AHE, we extract the anomalous Hall resistivity  $\rho_{xy}^A$  and the ordinary Hall effect  $R_0\mu_0H$  from the linear fit of  $\rho_{xy}$  in the field range of 3 to 9 T using the expression  $\rho_{xy} = R_0\mu_0H + \rho_{xy}^A$ . The ordinary Hall coefficient  $R_0$  allows us to calculate the carrier density  $n$ . The anomalous Hall resistivity  $\rho_{xy}^A$  is converted to the AHC  $\sigma_{xy}^A$  via the expression  $\sigma_{xy}^A = \rho_{xy}^A / (\rho_{xy}^A{}^2 + \rho_{xx}^2)$ , where the values of  $\rho_{xx}$  are taken at 9 T, at which the magnetic moments are most aligned along the  $c$  axis. Using  $\rho_{xx}$  at different fields results in minor changes in the absolute values of the AHC but does not change its dependence on carrier density or longitudinal conductivity. Figures 3(b) and 3(c) show the temperature dependence of the carrier density  $n$  and AHC  $\sigma_{xy}^A$  between 2 and 100 K. Intriguingly, the carrier densities of all three samples show a nonmonotonic temperature dependence, which is in contrast to the thermally activated behavior where carrier density decreases monotonically with temperature. This is likely due to the interplay between the thermal activation of carriers and the change in magnetic configurations at elevated temperatures due to moment fluctuations. Regardless of the origin, the carrier density and the AHC measured across three samples show a substantial variation for  $T < T_N$ , providing us an opportunity to systematically investigate the carrier density dependence of AHC of  $\text{EuCd}_2\text{As}_2$  in the field-induced FM state.

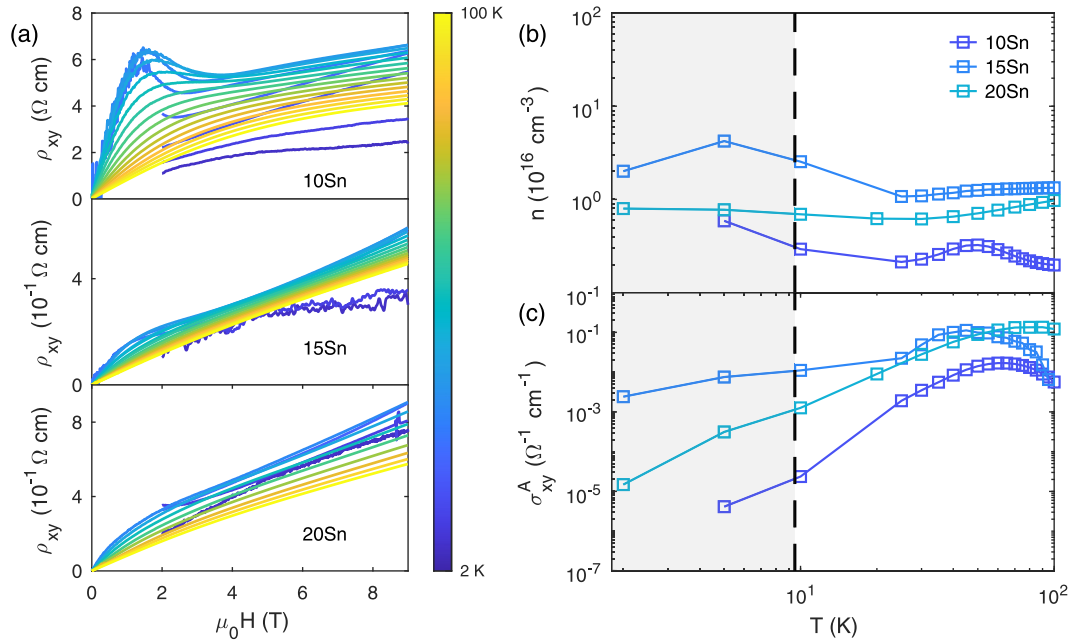


FIG. 3. The temperature dependence of the carrier density and anomalous Hall conductivity of  $\text{EuCd}_2\text{As}_2$ . (a) Hall resistivity  $\rho_{xy}$  versus magnetic field for samples from 10Sn, 15Sn, and 20Sn at temperatures between 2 and 100 K. (b) Carrier density  $n$  and (c) anomalous Hall conductivity  $\sigma_{xy}^A$  versus temperature obtained by fitting from  $\rho_{xy}$  in (a) (see text for details of the fitting). Vertical lines mark antiferromagnetic transition temperature  $T_N = 9.5 \text{ K}$ .

In a Weyl semimetal, the Weyl nodes are the source and sink of Berry curvature flux in the momentum space. In an ideal time-reversal symmetry-breaking Weyl semimetal, the single pair of Weyl nodes forms a Berry curvature dipole and gives rise to an intrinsic AHE solely depending on the separation of the Weyl nodes,  $\sigma_{xy}^A = (e^2/2\pi h \Delta k)$ . This  $\sigma_{xy}^A$  is topological and independent of the Fermi level position; hence, we should expect a constant AHC even if the carrier density approaches zero. Here, we compile the data of  $\sigma_{xy}^A$  and  $n$  extracted below 10 K in the field range of 3–9 T when  $\text{EuCd}_2\text{As}_2$  is in the field-induced FM state from Figs. 3(b) and 3(c) and plot the result in Fig. 4(a) on a log-log scale. In addition to the data collected in this work (blue squares),

the AHC measured from higher carrier density samples in previous works are also included [3,13–15]. The horizontal black dashed line indicates the value of the intrinsic AHC,  $\sim 30 \Omega^{-1} \text{ cm}^{-1}$ , from a single pair of Weyl points separated by  $0.52 \text{ nm}^{-1}$  in ferromagnetic  $\text{EuCd}_2\text{As}_2$  predicted by previous DFT calculations [3,4]. As shown in Fig. 4(a), the observed  $\sigma_{xy}^A$  has a strong dependence on carrier density  $n$  and decreases dramatically as  $n$  decreases. As the carrier density approaches  $\sim 10^{15} \text{ cm}^{-3}$ , the AHC reaches a value that is 5 orders of magnitude smaller than the AHC expected for an ideal Weyl semimetal.

To gain insight into the underlying mechanism of the AHE in  $\text{EuCd}_2\text{As}_2$ ,  $\sigma_{xy}^A$  versus  $\sigma_{xx}$  [ $\sigma_{xx} = \rho_{xx}/(\rho_{xy}^2 + \rho_{xx}^2)$ ] is plotted

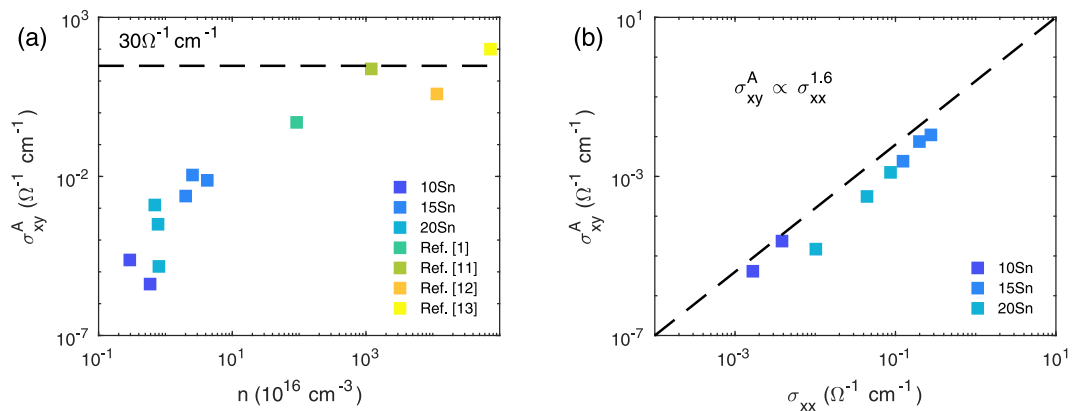


FIG. 4. Carrier density dependence and the scaling relationship of the anomalous Hall effect in  $\text{EuCd}_2\text{As}_2$ . (a) Anomalous Hall conductivity  $\sigma_{xy}^A$  versus carrier density  $n$  measured from samples 10Sn, 15Sn, and 20Sn and semimetallic  $\text{EuCd}_2\text{As}_2$  reported in previous works [3,13–15]. The expected value of  $\sigma_{xy}^A$  (black dashed line) is for an ideal Weyl semimetal with only one pair of Weyl nodes separated by  $0.52 \text{ nm}^{-1}$  [3]. (b) Anomalous Hall conductivity  $\sigma_{xy}^A$  versus longitudinal conductivity  $\sigma_{xx}$  in log-log scale. The dashed line marks the power law  $\sigma_{xy}^A \propto \sigma_{xx}^{1.6}$ .

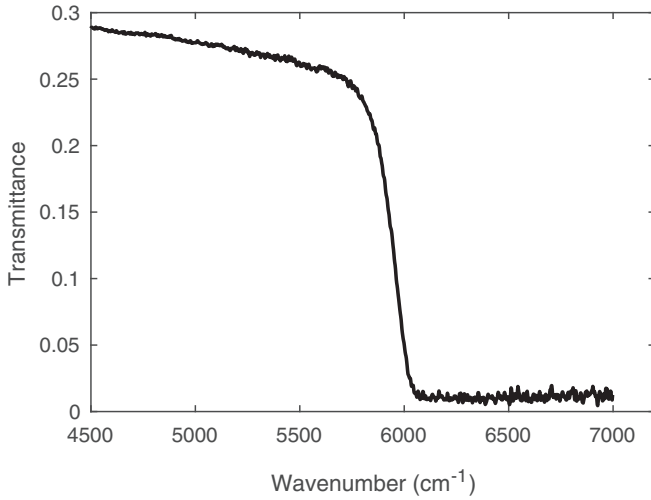


FIG. 5. Transmittance spectrum of  $\text{EuCd}_2\text{As}_2$ . Transmittance versus incident light wave number of sample 10Sn measured by FTIR at room temperature. The incident lights with a wave number larger than  $6000 \text{ cm}^{-1}$  are fully absorbed, consistent with a band gap of  $0.74 \text{ eV}$ .

in Fig. 4(b). Note that we use the values of resistivity tensors at  $\mu_0 H = 9 \text{ T}$  for all conversions since both longitudinal and Hall resistivities depend strongly on the magnetic fields. As shown in Fig. 4(b), all longitudinal conductivities  $\sigma_{xx}$  fall below the value of  $1 \Omega^{-1} \text{ cm}^{-1}$ , which belongs to the insulating regime, where conduction and the AHE are governed by the variable-range hopping or activated hopping process. Moreover, the AHC versus longitudinal conductivity can be well fitted by a power law relation,  $\sigma_{xy}^A \propto \sigma_{xx}^\alpha$ , with  $\alpha = 1.6$  (black dashed line). This is consistent with previous experimental results and theoretical models of the AHE in the insulating regime [25]. Thus, the observed AHC is fully consistent with  $\text{EuCd}_2\text{As}_2$  being a magnetic semiconductor.

#### D. Optical transmittance

As a final confirmation, the optical transmittance spectrum of sample 10Sn was measured using the Fourier transform infrared spectroscopy (FTIR) technique at room temperature. As shown in Fig. 5,  $\text{EuCd}_2\text{As}_2$  remains transparent up to a wave number of  $6000 \text{ cm}^{-1}$  (equivalent to  $\sim 0.74 \text{ eV}$ ), followed by a sharp drop in transmittance at higher wave numbers. This is consistent with the presence of an  $\sim 0.74 \text{ eV}$  band gap, which is in agreement with the optical study reported in Ref. [18].

### III. DISCUSSION

The comprehensive anomalous Hall effect and optical transmittance measurements presented above clearly support the conclusion that  $\text{EuCd}_2\text{As}_2$  is a magnetic semiconductor. One remaining question is why most of the previous first-principles calculations identified ferromagnetic  $\text{EuCd}_2\text{As}_2$  as a Weyl semimetal. We note that recent calculations by Cuono *et al.* [19] showed that electron correlation effects can significantly alter the electronic and topological behaviors of  $\text{EuCd}_2\text{As}_2$ . In particular, within the standard

generalized gradient approximation (GGA) functional, AFM  $\text{EuCd}_2\text{As}_2$  can exhibit a vanishing electronic band gap and nontrivial band topology only when Eu's on-site Hubbard repulsion  $\mathbf{U}$  is less than  $\sim 6 \text{ eV}$  [19]. Previous theoretical and experimental studies considered  $\mathbf{U}$  values in the range of  $\sim 3 - 5 \text{ eV}$  [5,7,12,17,26,27], which could tend to lead to the conclusion that  $\text{EuCd}_2\text{As}_2$  is topologically nontrivial. Since the Hubbard repulsion plays a critical role, it is important to more accurately estimate the  $\mathbf{U}$  value.

Here, we employ the linear-response ansatz by Cococcioni and de Gironcoli to determine the Hubbard  $\mathbf{U}$  from first principles [28]. In this approach, the  $\mathbf{U}$  value is derived by measuring the change in the Eu  $f$  orbital occupation as a response to external perturbation of an on-site potential. Specifically, after an initial DFT ground state calculation, the self-consistent response  $\chi$  and non-self-consistent response  $\chi_0$  are constructed by computing the orbital occupation change with and without DFT charge density updates, respectively. Afterward,  $\mathbf{U}$  is determined by subtracting the inverse of the self-consistent response from the non-self-consistent one:  $\mathbf{U} = \chi^{-1} - \chi_0^{-1}$ . Figure 6(a) shows the corresponding calculation on a five-atom  $\text{EuCd}_2\text{As}_2$  unit cell in the external potential range  $-0.20$  to  $0.20 \text{ eV}$ . When the perturbation is small, both response functions show a linear trend, so  $\chi^{-1}$  and  $\chi_0^{-1}$  can be obtained directly from the linear slopes. With a larger perturbation, the response functions may exhibit a nonlinear behavior. In this case, the linear-response approach can still be applied by using a nonlinear fit and then taking the derivative near the zero potential [29]. The result is essentially equivalent to that of a linear fit in a smaller perturbation regime.

As seen in Fig. 6(a), the Hubbard  $\mathbf{U}$  for a five-atom  $\text{EuCd}_2\text{As}_2$  unit cell is calculated to be  $6.77 \text{ eV}$ . Since the  $\mathbf{U}$  value is largely affected by charge screening, it is necessary to examine the convergence in larger DFT supercells. We performed corresponding linear-response  $\mathbf{U}$  calculations up to a unit cell of 40 atoms, where the  $\mathbf{U}$  value is found to converge to  $\sim 8 \text{ eV}$ , as shown in Fig. 6(b). We also performed the calculations using different DFT ground states, including paramagnetic (PM) and AFM, and found that the resulting  $\mathbf{U}$  values differ by less than  $\sim 0.1 \text{ eV}$ . In this regard, magnetism has only a small effect on the resulting  $\mathbf{U}$  value of  $\sim 8 \text{ eV}$ , which remains substantial in both the PM and AFM states. Unlike the empirical values of  $\mathbf{U} \sim 3-5 \text{ eV}$  considered in the literature [5,7,12,17,26], the strong Hubbard repulsion  $\mathbf{U} \sim 8 \text{ eV}$  discovered in our *ab initio* calculations thereby suggests a finite energy gap and only trivial band topology in  $\text{EuCd}_2\text{As}_2$ . We also note that a meta-GGA or hybrid DFT functional would lead to an ever larger energy gap that further suppresses the topological behavior [19]. Therefore, in accord with our carrier-control transport experiments, the theoretical results also indicate that  $\text{EuCd}_2\text{As}_2$  is likely to be a topologically trivial magnetic semiconductor.

### IV. CONCLUSION

Our study revealed that the carrier density dependence of the anomalous Hall conductivity in  $\text{EuCd}_2\text{As}_2$  does not align with the expected behavior of an ideal Weyl semimetal. Instead, the scaling relationship between the AHC and

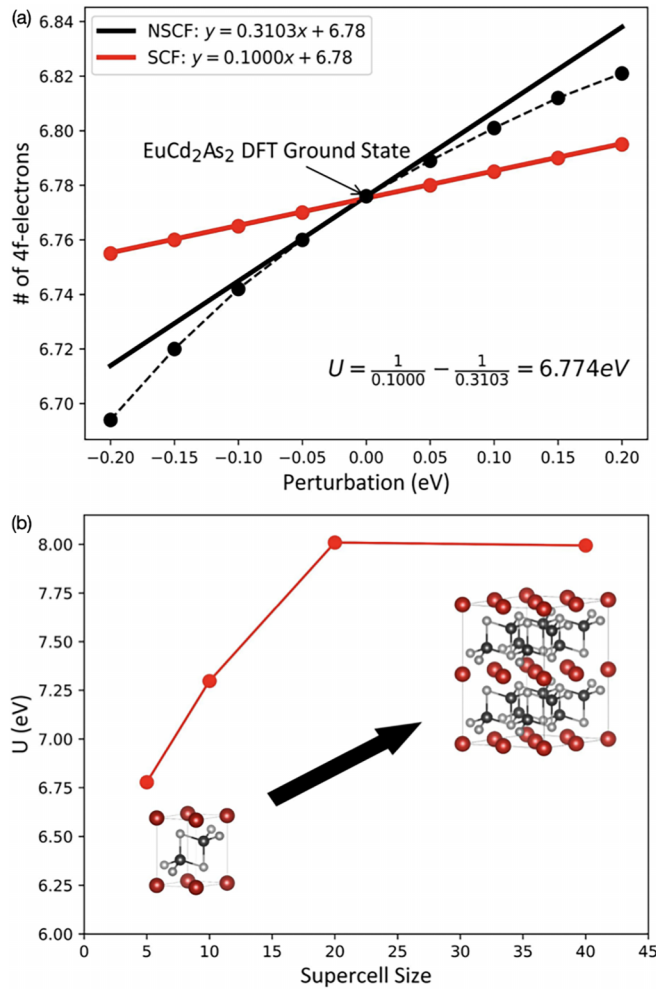


FIG. 6. First-principles linear-response calculations for the Hubbard  $U$  of Eu atoms in  $\text{EuCd}_2\text{As}_2$ . (a) Fitted charge self-consistent (solid red line) and non-self-consistent (solid black line) linear-response functions for a five-atom  $\text{EuCd}_2\text{As}_2$  unit cell. The inverse slopes of the response functions in the linear regime can be utilized to determine the  $U$  value. (b) Convergence test of the calculated Hubbard  $U$  parameter with respect to the supercell size. The results converge to  $U \sim 8$  eV in a 40-atom  $\text{EuCd}_2\text{As}_2$  unit cell. Such a strong  $U \sim 8$  eV would lead to a finite energy gap and suppression of the topological behavior in  $\text{EuCd}_2\text{As}_2$ .

longitudinal conductivity is in good agreement with the characteristics of insulating hopping transport. These observations, coupled with the substantial electronic gap revealed in the optical transmittance measurement, unambiguously establish that  $\text{EuCd}_2\text{As}_2$  is a magnetic semiconductor instead of a Weyl semimetal. We further performed *ab initio* calculations and discovered that the underestimation of Hubbard  $U$  could play a key role in previous misidentification of the topological phase in this material system. Despite being topologically trivial, the resistivity of  $\text{EuCd}_2\text{As}_2$  is extremely sensitive to the magnetic configuration of Eu-ordered moments, leading to a colossal magnetoresistance effect, indicative of a strong coupling between the electronic band gap and the magnetic orders. This unusual property may be useful for applications in spintronics and magneto-optoelectronics.

## V. METHODS

### A. Crystal synthesis

$\text{EuCd}_2\text{As}_2$  single crystals were synthesized via the Sn flux method [9]. Stoichiometric Eu, Cd, and As shots with 10, 15, 20, and 25 times atomic mass Sn shots were ground, mixed, and loaded in the bottom of a Canfield crucible [30]. Then the crucible was loaded in a quartz tube. To avoid oxidation, grind and load were conducted in the glove box filled with argon, and the ball valve was used to keep input materials from the air when taking them out of the glove box. The mixture was sealed in an evacuated quartz tube and placed in a box furnace. The mixture was heated to  $900^\circ\text{C}$  over 12 h, held for 24 h, and then slowly cooled over 200 h to  $550^\circ\text{C}$ . The tube was removed from the furnace and spun in a centrifuge to remove the Sn flux. This process yields platelike single crystals with a hexagonal shape up to a few millimeters in size. We discovered that the residual carrier density of crystals is highly sensitive to the ratio of Sn flux in the starting materials. The stoichiometric Eu pieces and Cd and As shots were mixed with 10 to 25 times atomic mass Sn shots as starting materials, which yielded  $\text{EuCd}_2\text{As}_2$  crystals with hole carrier density spanning from  $10^{15}$  to  $10^{16}$   $\text{cm}^{-3}$ . This allowed us to use various carrier densities as a convenient knob to study the electronic band structure of  $\text{EuCd}_2\text{As}_2$ .

### B. Materials characterization

The composition of all batches of crystals was determined by elemental analysis on a clean crystalline surface using a Sirion XL30 scanning electron microscope. All batches of crystals exhibited nearly perfect stoichiometric composition. A subset of crystals was crushed into fine powder and characterized by powder x-ray diffraction using a Rigaku MiniFlex at room temperature. The obtained crystal structure and lattice constants of all batches of crystals are identical to those in previous reports [8].

### C. Transport measurement

For transport measurements, the sample was cut into a rectangular plate using a wire saw and then made into a standard six-probe contact configuration with the current direction in plane and the magnetic field out of plane ( $c$  axis). The contact resistance of samples was limited to a few hundred  $\Omega$ , which was achieved by sputtering gold pads on the sample surface and adhering gold wires with sliver paste. The magnetotransport measurements were carried out in a 9 T physical property measurement system (PPMS). We utilized a Keithley2450 as the current source and voltmeter for measuring the  $\text{G}\Omega$  level resistance, benefiting from the high impedance resistance of the Keithley2450. However, the current source and measured voltage range should be adjusted accordingly to get a better signal as the resistivity changes a few orders of magnitude as temperature decreases in a short time. To eliminate any effects from contact misalignment, the magnetoresistance and Hall resistance were symmetrized and anti-symmetrized, respectively. Magnetization measurements were made using the vibrating sample magnetometry option of the PPMS.

### D. Optical measurement

FTIR spectroscopy was conducted using a Hyperion 2000 system from Bruker Inc. The measurement was performed in the transmission mode, employing an infrared globar source and a liquid-nitrogen-cooled mercury cadmium telluride (MCT) detector. To ensure optimal signal transmission, a thin crystal with a flat and clean surface was utilized. Additionally, a reference measurement was conducted using a silicon wafer.

### E. DFT calculation

DFT calculations were performed based on the plane wave pseudopotential software VASP (Vienna Ab initio Simulation Package) [31,32]. The calculations utilized the Perdew-Burke-Ernzerhof generalized gradient approximation functional [33] and the projector augmented wave basis [34,35]. Spin-orbit coupling was also included. A theoretically relaxed  $\text{EuCd}_2\text{As}_2$  crystal structure was considered, with the lattice parameters  $a = 4.45 \text{ \AA}$  and  $c = 7.35 \text{ \AA}$ , which are within 1% error compared to the experimental cell [6,10]. Convergence tests with respect to the plane wave cutoff energy and  $k$ -grid size were conducted. The calculations were converged with a cutoff energy of 600 eV, using the global break condition of  $10^{-6}$  eV in the electronic self-consistent loops. For the largest 40-atom unit cell under study, a  $9 \times 9 \times 5$   $k$  grid was adopted, which corresponds to a fine  $k$  points per reciprocal atom value of 16 200. The DFT ground states provide the input charge densities and wave functions for subsequent *ab initio* linear-response U calculations [28] to determine the Hubbard U value of Eu atoms.

Source data for this paper are available at [36]. All other data that support the plots within this paper and other findings of this study are available from the corresponding author upon reasonable request.

### ACKNOWLEDGMENTS

This work was mainly supported by the Air Force Office of Scientific Research (AFOSR) under Award No. FA2386-21-1-4060. The transport experiment was partially supported as part of Programmable Quantum Materials, an Energy Frontier Research Center funded by the U.S. Department of Energy (DOE), Office of Science, Basic Energy Sciences (BES), under Award No. DE-SC0019443. The FTIR measurement was supported by NSF MRSEC at UW (Grant No. DMR-2308979). J.-H.C. and X.X. acknowledge the support from the State of Washington funded Clean Energy Institute. J.-H.C. also acknowledges support from the David and Lucile Packard Foundation. A portion of this work was performed at the National High Magnetic Field Laboratory, which is supported by National Science Foundation (NSF) Cooperative Agreement No. DMR-1644779 and the state of Florida. The calculations were performed on the Frontera computing system at the Texas Advanced Computing Center made possible by NSF Award No. OAC-1818253.

### APPENDIX

#### 1. Refinement of x-ray diffraction

The x-ray diffraction pattern was obtained from a Rigaku MiniFlex diffractometer as described in Sec. V. The observed x-ray diffraction intensity pattern of crystals from

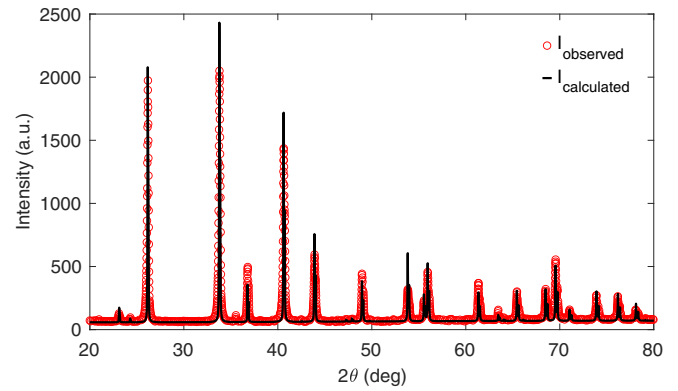


FIG. 7. Refinement of powder x-ray diffraction of  $\text{EuCd}_2\text{As}_2$ . The observed x-ray diffraction spectrum and the calculated intensity gained by the Rietveld refinement.

10Sn  $\text{EuCd}_2\text{As}_2$  are shown in Fig. 7, along with the calculated intensity made via the Rietveld refinement of observed intensity using the FULLPROF suite [37]. The crystal lattice constants from the refinement are  $a = 4.4386 \text{ \AA}$  and  $c = 7.3239 \text{ \AA}$ , which agree with the previous reports [6,7,9].

#### 2. High-field magnetoresistance

High-field magnetoresistance measurements were conducted under up to 35 T magnetic field at the National High Field Magnetic National Laboratory (NHMFL) in Tallahassee, Florida. Figure 8 shows  $\rho_{xx}$  measured on a sample from 10Sn  $\text{EuCd}_2\text{As}_2$  with the magnetic field along the  $c$  axis at 1.4 K. The magnetoresistivity presents a quadratic increase as field increases. No Shubnikov-de Haas quantum oscillations appears until 35 T.

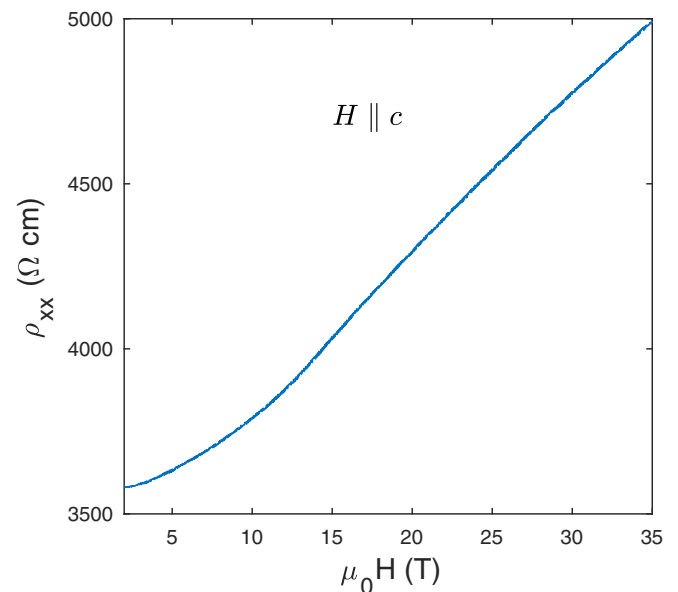


FIG. 8. High-field magnetoresistance. The magnetoresistivity  $\rho_{xx}$  versus along the  $c$ -axis magnetic field  $\mu_0 H$  ranges from 2 to 35 T of the sample from 10Sn  $\text{EuCd}_2\text{As}_2$ .

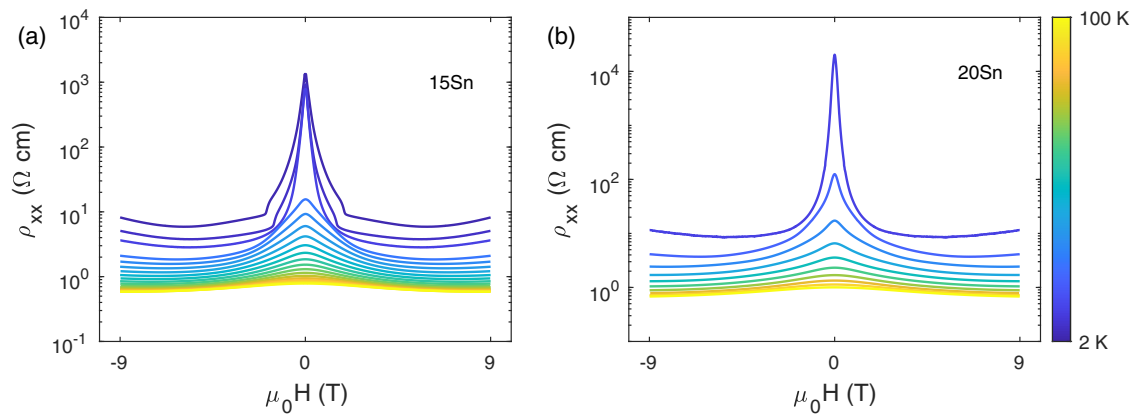


FIG. 9. Colossal magnetoresistance. Temperature dependence of resistivity  $\rho_{xx}$  versus  $\pm 9$  T magnetic field along the  $c$  axis at temperatures between 2 and 150 K for samples from (a) 15Sn and (b) 20Sn.

### 3. Magnetoresistance of samples from 15Sn and 20Sn

The magnetoresistivity  $\rho_{xx}$  as a function of field was also conducted on samples from 15Sn and 20Sn. Figure 9 shows  $\rho_{xx}$  versus magnetic field at fixed temperatures between 2 and

150 K. The behaviors are qualitatively the same as those of the represented data of the sample from 10Sn shown in the main text.

- [1] N. P. Armitage, E. J. Mele, and A. Vishwanath, Weyl and Dirac semimetals in three-dimensional solids, *Rev. Mod. Phys.* **90**, 015001 (2018).
- [2] B. Yan and C. Felser, Topological materials: Weyl semimetals, *Annu. Rev. Condens. Matter Phys.* **8**, 337 (2017).
- [3] J.-R. Soh, F. de Juan, M. G. Vergniory, N. B. M. Schröter, M. C. Rahn, D. Y. Yan, J. Jiang, M. Bristow, P. Reiss, J. N. Blandy, Y. F. Guo, Y. G. Shi, T. K. Kim, A. McCollam, S. H. Simon, Y. Chen, A. I. Coldea, and A. T. Boothroyd, Ideal Weyl semimetal induced by magnetic exchange, *Phys. Rev. B* **100**, 201102(R) (2019).
- [4] L.-L. Wang, N. H. Jo, B. Kuthanazhi, Y. Wu, R. J. McQueeney, A. Kaminski, and P. C. Canfield, Single pair of Weyl fermions in the half-metallic semimetal  $\text{EuCd}_2\text{As}_2$ , *Phys. Rev. B* **99**, 245147 (2019).
- [5] J.-Z. Ma *et al.*, Spin fluctuation induced Weyl semimetal state in the paramagnetic phase of  $\text{EuCd}_2\text{As}_2$ , *Sci. Adv.* **5**, eaaw4718 (2019).
- [6] H. P. Wang, D. S. Wu, Y. G. Shi, and N. L. Wang, Anisotropic transport and optical spectroscopy study on antiferromagnetic triangular lattice  $\text{EuCd}_2\text{As}_2$ : An interplay between magnetism and charge transport properties, *Phys. Rev. B* **94**, 045112 (2016).
- [7] M. C. Rahn, J.-R. Soh, S. Francoual, L. S. I. Veiga, J. Stremperfer, J. Mardegan, D. Y. Yan, Y. F. Guo, Y. G. Shi, and A. T. Boothroyd, Coupling of magnetic order and charge transport in the candidate Dirac semimetal  $\text{EuCd}_2\text{As}_2$ , *Phys. Rev. B* **97**, 214422 (2018).
- [8] I. Schellenberg, U. Pfannenschmidt, M. Eul, C. Schwickert, and R. Pöttgen, A  $^{121}\text{Sb}$  and  $^{151}\text{Eu}$  mössbauer spectroscopic investigation of  $\text{EuCd}_2\text{X}_2$  ( $X = \text{P}, \text{As}, \text{Sb}$ ) and  $\text{YbCd}_2\text{Sb}_2$ , *Z. Anorg. Allge. Chem.* **637**, 1863 (2011).
- [9] N. H. Jo, B. Kuthanazhi, Y. Wu, E. Timmons, T.-H. Kim, L. Zhou, L.-L. Wang, B. G. Ueland, A. Palasyuk, D. H. Ryan, R. J. McQueeney, K. Lee, B. Schrunck, A. A. Burkov, R. Prozorov, S. L. Bud'ko, A. Kaminski, and P. C. Canfield, Manipulating magnetism in the topological semimetal  $\text{EuCd}_2\text{As}_2$ , *Phys. Rev. B* **101**, 140402(R) (2020).
- [10] E. Gati, S. L. Bud'ko, L.-L. Wang, A. Valadkhani, R. Gupta, B. Kuthanazhi, L. Xiang, J. M. Wilde, A. Sapkota, Z. Guguchia, R. Khasanov, R. Valentí, and P. C. Canfield, Pressure-induced ferromagnetism in the topological semimetal  $\text{EuCd}_2\text{As}_2$ , *Phys. Rev. B* **104**, 155124 (2021).
- [11] K. M. Taddei, L. Yin, L. D. Sanjeeva, Y. Li, J. Xing, C. dela Cruz, D. Phelan, A. S. Sefat, and D. S. Parker, Single pair of Weyl nodes in the spin-canted structure of  $\text{EuCd}_2\text{As}_2$ , *Phys. Rev. B* **105**, L140401 (2022).
- [12] G. Hua, S. Nie, Z. Song, R. Yu, G. Xu, and K. Yao, Dirac semimetal in type-IV magnetic space groups, *Phys. Rev. B* **98**, 201116(R) (2018).
- [13] Y. Xu, L. Das, J. Z. Ma, C. J. Yi, S. M. Nie, Y. G. Shi, A. Tiwari, S. S. Tsirkin, T. Neupert, M. Medarde, M. Shi, J. Chang, and T. Shang, Unconventional transverse transport above and below the magnetic transition temperature in Weyl semimetal  $\text{EuCd}_2\text{As}_2$ , *Phys. Rev. Lett.* **126**, 076602 (2021).
- [14] X. Cao, J.-X. Yu, P. Leng, C. Yi, X. Chen, Y. Yang, S. Liu, L. Kong, Z. Li, X. Dong, Y. Shi, M. Bibes, R. Peng, J. Zang, and F. Xiu, Giant nonlinear anomalous Hall effect induced by spin-dependent band structure evolution, *Phys. Rev. Res.* **4**, 023100 (2022).
- [15] S. Roychowdhury, M. Yao, K. Samanta, S. Bae, D. Chen, S. Ju, A. Raghavan, N. Kumar, P. Constantinou, S. N. Guin, N. C. Plumb, M. Romanelli, H. Borrmann, M. G. Vergniory, V. N. Strocov, V. Madhavan, C. Shekhar, and C. Felser, Anomalous Hall conductivity and Nernst effect of the ideal Weyl semimetallic ferromagnet  $\text{EuCd}_2\text{As}_2$ , *Adv. Sci.* **10**, 2207121 (2023).



- [16] Y. Wang *et al.*, Giant and reversible electronic structure evolution in a magnetic topological material  $\text{EuCd}_2\text{As}_2$ , *Phys. Rev. B* **106**, 085134 (2022).
- [17] J. Ma, H. Wang, S. Nie, C. Yi, Y. Xu, H. Li, J. Jandke, W. Wulfhchel, Y. Huang, D. West, P. Richard, A. Chikina, V. N. Strocov, J. Mesot, H. Weng, S. Zhang, Y. Shi, T. Qian, M. Shi, and H. Ding, Emergence of nontrivial low-energy Dirac fermions in antiferromagnetic  $\text{EuCd}_2\text{As}_2$ , *Adv. Mater.* **32**, 1907565 (2020).
- [18] D. Santos-Cottin *et al.*,  $\text{EuCd}_2\text{As}_2$ : A magnetic semiconductor, *Phys. Rev. Lett.* **131**, 186704 (2023).
- [19] G. Cuono, R. M. Sattigeri, C. Autieri, and T. Dietl, Ab initio overestimation of the topological region in Eu-based compounds, *Phys. Rev. B* **108**, 075150 (2023).
- [20] K.-Y. Yang, Y.-M. Lu, and Y. Ran, Quantum Hall effects in a Weyl semimetal: Possible application in pyrochlore iridates, *Phys. Rev. B* **84**, 075129 (2011).
- [21] A. A. Burkov, Anomalous Hall effect in Weyl metals, *Phys. Rev. Lett.* **113**, 187202 (2014).
- [22] Y. Wang, J. Ma, J. Yuan, W. Wu, Y. Zhang, Y. Mou, J. Gu, P. Cheng, W. Shi, X. Yuan, J. Zhang, Y. Guo, and C. Zhang, Absence of metallicity and bias-dependent resistivity in low-carrier-density  $\text{EuCd}_2\text{As}_2$ , *Sci. China Phys. Mech. Astron.* **67**, 247311 (2024).
- [23] A. P. Ramirez, Colossal magnetoresistance, *J. Phys.: Condens. Matter* **9**, 8171 (1997).
- [24] G. Wang, G. Chang, H. Zhou, W. Ma, H. Lin, M. Z. Hasan, S.-Y. Xu, and S. Jia, Field-induced metal-insulator transition in  $\beta\text{-EuP}_3$ , *Chin. Phys. Lett.* **37**, 107501 (2020).
- [25] N. Nagaosa, J. Sinova, S. Onoda, A. H. MacDonald, and N. P. Ong, Anomalous Hall effect, *Rev. Mod. Phys.* **82**, 1539 (2010).
- [26] J. Krishna, T. Nautiyal, and T. Maitra, First-principles study of electronic structure, transport, and optical properties of  $\text{EuCd}_2\text{As}_2$ , *Phys. Rev. B* **98**, 125110 (2018).
- [27] Z. Yu, X. Chen, W. Xia, N. Wang, X. Lv, X. Liu, H. Su, Z. Li, D. Wu, W. Wu, Z. Liu, J. Zhao, M. Li, S. Li, X. Li, Z. Dong, C. Zhou, L. Zhang, X. Wang, N. Yu, Z. Zou, J. Luo, J. Cheng, L. Wang, Z. Zhong, and Y. Guo, Structure, magnetotransport, and theoretical study on the layered antiferromagnet topological Phase  $\text{EuCd}_2\text{As}_2$  under higher pressure, *Adv. Quantum Technol.* **6**, 2200128 (2023).
- [28] M. Cococcioni and S. de Gironcoli, Linear response approach to the calculation of the effective interaction parameters in the LDA + U method, *Phys. Rev. B* **71**, 035105 (2005).
- [29] D. S. Lambert and D. D. O'Regan, Use of DFT + U + J with linear response parameters to predict non-magnetic oxide band gaps with hybrid-functional accuracy, *Phys. Rev. Res.* **5**, 013160 (2023).
- [30] P. C. Canfield, T. Kong, U. S. Kaluarachchi, and N. H. Jo, Use of frit-disc crucibles for routine and exploratory solution growth of single crystalline samples, *Philos. Mag.* **96**, 84 (2016).
- [31] G. Kresse and J. Furthmüller, Efficient iterative schemes for *ab initio* total-energy calculations using a plane-wave basis set, *Phys. Rev. B* **54**, 11169 (1996).
- [32] J. F. G. Kresse, Efficiency of ab-initio total energy calculations for metals and semiconductors using a plane-wave basis set, *Comput. Mater. Sci.* **6**, 15 (1996).
- [33] J. P. Perdew, K. Burke, and M. Ernzerhof, Generalized gradient approximation made simple [Phys. Rev. Lett. **77**, 3865 (1996)], *Phys. Rev. Lett.* **78**, 1396(E) (1997).
- [34] P. E. Blöchl, Projector augmented-wave method, *Phys. Rev. B* **50**, 17953 (1994).
- [35] G. Kresse and D. Joubert, From ultrasoft pseudopotentials to the projector augmented-wave method, *Phys. Rev. B* **59**, 1758 (1999).
- [36] <https://github.com/yoyos456/PRB14204.git>.
- [37] J. Rodríguez-Carvajal, Recent advances in magnetic structure determination by neutron powder diffraction, *Phys. B (Amsterdam, Neth.)* **192**, 55 (1993).